crystals

MDPI

Article

Microstructure and Kinetics of Thermal Behavior of Martensitic Transformation in (Mn,Ni)Sn Heusler Alloy

Hanen Rekik [1], Bechir Hammami [2], Mohamed Khitouni [1,2,*], Tarek Bachagha [1], Joan-Josep Suñol [3] and Mahmoud Chemingui [1]

[1] Laboratory of Inorganic Chemistry (LR-17-ES-07), Faculty of Science, University of Sfax, Sfax 3018, Tunisia
[2] Department of Chemistry, College of Science, Qassim University, Buraidah 51452, Saudi Arabia
[3] Department of Physics, Campus Montilivi, University of Girona, 17071 Girona, Spain
* Correspondence: kh.mohamed@qu.edu.sa

Abstract: In this work, scanning electron microscopy, X-ray diffraction, and differential scanning calorimetry were used to investigate the solidification structure, thermal behavior, and kinetics of the martensitic transformations of the (Mn,Ni)Sn as-spun and annealed ribbons synthesized by melt-spinning. At room temperature, the as-spun and annealed (Mn,Ni)Sn ribbons exhibited a cubic single-phase Heusler $L2_1$ structure. The kinetics of the martensitic transformation (MT) was studied, together with their microstructure evolution and cooling rate dependence. The mechanism was also investigated. Additionally, a high dependence between the cooling rates and energy activation (Ea) was detected. A more detailed characterization of MT and account of thermodynamic parameters were examined after annealing.

Keywords: Heusler alloys; rapid solidification; martensitic transition; thermal analysis; energy activation; kinetics

Citation: Rekik, H.; Hammami, B.; Khitouni, M.; Bachagha, T.; Suñol, J.-J.; Chemingui, M. Microstructure and Kinetics of Thermal Behavior of Martensitic Transformation in (Mn,Ni)Sn Heusler Alloy. *Crystals* **2022**, *12*, 1644. https://doi.org/10.3390/cryst12111644

Academic Editor: Shouxun Ji

Received: 20 October 2022
Accepted: 13 November 2022
Published: 16 November 2022

1. Introduction

The reversible first-order martensitic transition (MT) in Heusler Ni–Mn–X (X = Ga, Sn, In, and Sb) materials has garnered a lot of interest [1–4]. In these systems, MT occurs between a martensite phase with both a clearly reduced magnetic susceptibility and diversity of structural configurations and the ferromagnetic austenite phase, which has the cubic $L2_1$ structure. This latter structure, which can be 10M, 14M, 4O, or $L1_0$ structures, varies in composition and fabrication techniques [5]. Recent research demonstrated the efficiency of the melt-spinning process in producing highly textured, homogeneous, polycrystalline ribbons [6,7] with significantly improved magnetic characteristics [8]. As compared to those obtained through conventional casting, the rapid solidification of alloys via the melt-spinning technique can result in improved mechanical properties [9]. A nonequilibrium position of the atoms may also be caused by rapid solidification from the liquid phase. This makes it possible to change the atomic order, making research into melt-spun ribbon materials very important. Recently, some intriguing findings on the Ni–Mn–X alloy ribbons' physical characteristics were published. According to Hernando et al. [10], the martensite phase that forms in Ni–Mn–X ribbons has a different crystal structure than materials that are arc-melted in bulk. In comparison to the bulk alloy, the Heusler Ni–Mn–X ribbons' MT always starts at a lower temperature. For instance, Krenke et al. [11] reported that the martensitic transformation of $Ni_{50}Mn_{37}Sn_{13}$ ribbons occurred in the range of 300 K, but Santos et al. [12] observed that the change took place at around 212 K. The reduced degree of atomic order and internal tension introduced during rapid solidification, according to Feng et al. [13], explained why the transition temperature of the $Ni_{50}Mn_{28+x}Ga_{22-x}$ (x = 0, 1, 2, 3) ribbons is approximately 10 K lower than that of the corresponding bulk alloys. The alloy composition, preparation conditions, and external parameters can be used to control the MT temperatures in ternary

Ni–Mn–X (X = In, Sn, and Sb) alloys (magnetic field and hydrostatic pressure [14]). It has been suggested that a multitude of factors can affect the value of MT temperatures. By varying the composition or substituting 3*d* transition metals such as Cr, Fe, Co, and Cu, the valence electron concentration (e/a) and MT temperatures can be changed [15–18]. The variation in electron concentration and the Mn–Mn interatomic distance are also responsible for the compositional dependence of the phase-transition temperature [19,20]. However, superior physical properties with potential applications originating from first-order magnetic-induced martensite transformation, e.g., inverse magnetocaloric effect [21] and large magnetoresistance [22], have been reported to be comparable to bulk alloys. Additionally, it has been found that annealing for a short time [21] can significantly improve the physical properties of ribbons. Moreover, many fundamental aspects associated with the melt-spun rapid solidification process remain unclear, and research on Mn–Ni–X ribbons is still in its early stages; aspects under investigation include rapidly solidified phase competition and selection, microstructures, nonequilibrium thermodynamics, and kinetics of solid-phase transition. It is necessary to perform more studies to promote the potential applications of these materials.

At present, no studies on the effect of annealing on the MT of $Mn_{51}Ni_{39}Sn_{10}$ (at.%) alloy have been performed. Thus, the purpose of this study is to investigate the impact of annealing on the modification of the microstructure and the behavior of phase transformation temperatures of Heusler $Mn_{51}Ni_{39}Sn_{10}$ alloy.

2. Experimental Procedure

High-purity (99.99%) constituent metals were used to produce the as-cast ingots with the nominal composition $Mn_{51}Ni_{39}Sn_{10}$ utilizing the Bühler MAM-1 compact arc melting process. To ensure good initial homogeneity, these alloys experienced four melting cycles. With a circular nozzle of 0.5 mm and an argon overpressure, the samples were induction-melted in quartz crucibles before being ejected onto the polished surface of a copper wheel rotating at a linear speed of 48 ms^{-1} (Figure 1). The obtained as-quenched ribbons were flakes having dimensions of 1.2–2.0 mm in width and 4–12 mm in length. The ribbons were fixed in a quartz tube filled with argon gas, followed by annealing at 1273 K for 1 h, and then quenched in ice water. Following that, obtained samples were named as-spun and annealed. Scanning electron microscopy (SEM) was used on a ZEISS DSM-960A microscope fitted with an X-ray energy dispersive spectroscopy (EDS) microanalysis system to analyze the microstructure and elemental compositions. At room temperature (RT), the materials' structural characteristics were determined using X-ray diffractograms (XRD) on a Siemens D500 X-ray powder diffractometer with Cu–Kα radiation (λ = 1.5418 Å). Using the Maud Program, the sample structures were determined [23]. Calorimetry was used to verify the structural transformation of austenite to martensite. Under a nitrogen atmosphere, the cyclic tests (cooling–heating) were recorded at various rates of 10, 15, 20, 30, and 40 K/min. The Mettler-Toledo DSC30 device was used to perform DSC scans below RT while using a liquid nitrogen cooling system. The phase-transition activation energy was determined based on the DSC measurements after these measurements were used to analyze the typical temperatures of MT.

(**a**) (**b**)

Figure 1. (**a**) Melt-spun chamber and (**b**) the obtained as-quenched ribbons.

3. Results and Discussion

3.1. SEM Analysis

The typical SEM images of the wheel surface of (Mn,Ni)Sn alloy are presented in Figure 2a. The austenite structure's granular microstructure is clearly visible on the wheel surface. This ribbon easily cleaves along this usual direction because it is mechanically weak and brittle. In Figure 2b, the alloy's free surface is also shown. These samples, which were obtained at high quenching rates, had a microstructure that was granular and completely crystalline. Around 1–2 μm was the value for the typical grain size. Furthermore, these typical grain size values are considerably lower than those seen in bulk alloys with coarse-grained microstructures and grain sizes ranging from 10 to 100 μm [1].

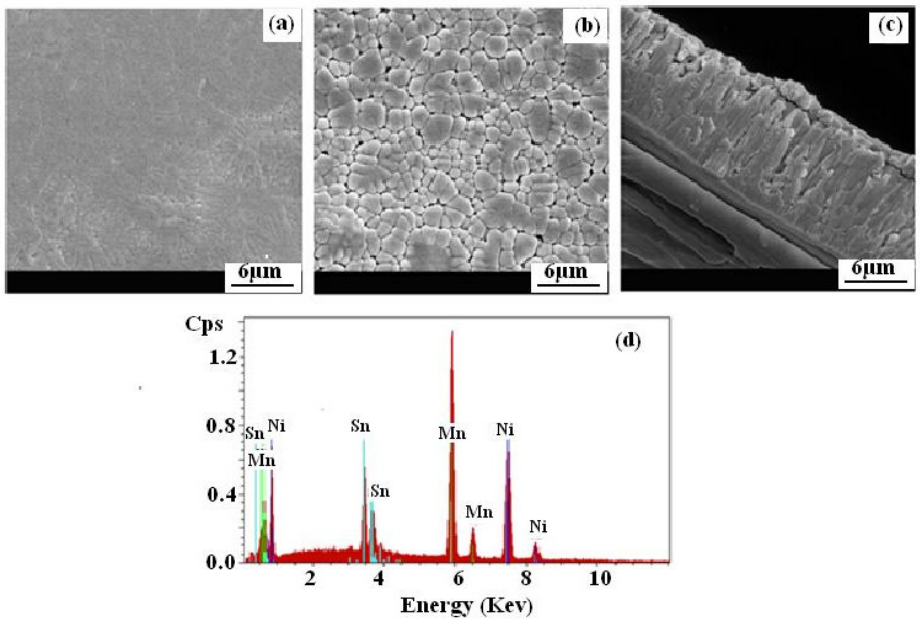

Figure 2. SEM images of wheel surface (**a**), free surface (**b**), and the cross-section microstructure (**c**) of the as-spun and annealed ribbons and the associated EDS analysis (**d**).

Figure 2c displays the cross-sections perpendicular to ribbon planes. The SEM images show that the samples were entirely crystalline. Additionally, a collinear granular columnar microstructure was visible. The ribbon was about 8 μm thick. With the longest axis aligned perpendicular to the ribbon plane, the thin layer of tiny equiaxed grains crystallized along the whole ribbon thickness. Figure 2d displays the results of the EDX analysis of the as-spun ribbon, confirming that mixed metallic elements were present. The nominal composition of the as-spun ribbon (51.2 at.% Ni; 39.3 at.% Mn; 9.5 at.% Sn) and the composition analysis results were in good accordance.

3.2. Structural Analysis

When choosing the parameters for a thermal study, it is frequently crucial to understand the crystal structure at RT [24]. The martensite–austenite transition must occur below RT in order to detect a cubic phase. On the other hand, if the phase is orthorhombic, monoclinic, or tetragonal, heating the alloy at normal temperature could produce the same transition. The XRD patterns of (Mn,Ni)Sn ribbons examined at RT are shown in Figure 3. Utilizing the Maud software program, miller indexes were assigned. After fitting, one can observe an austenite phase of the cubic $L2_1$ structure in both alloys. A crystalline structure cubic Heusler $L2_1$ structure, with lattice parameters of as-spun and annealed ribbons 5.995(1) and 5.990(1) Å, respectively, was confirmed by the reflections indexed as (311) and (331). On the basis of this XRD result, the martensite–austenite transition might be found using a DSC scan of the ribbon alloy that was cooled from RT. Recently, some interesting results on the physical characteristics of the Heusler Mn–Ni–Sn alloy were published. Coll et al. [24] reported that Mn–Ni–Sn alloys are completely single-phase at RT, with the cubic austenite phase thermally evolving into the structurally modulated orthorhombic martensite phase. However, the alloy's composition has a significant impact on the martensitic transition (MT). A single-phase $L2_1$ cubic austenite structure was seen at RT in a recent study using the as-spun $Ni_{50}Mn_{37}Sn_{6.5}In_{6.5}$ alloy [25], whereas the current phase in $Ni_{50}Mn_{42.5}Sn_{7.5}$ alloys is of the 14M monoclinic type [26].

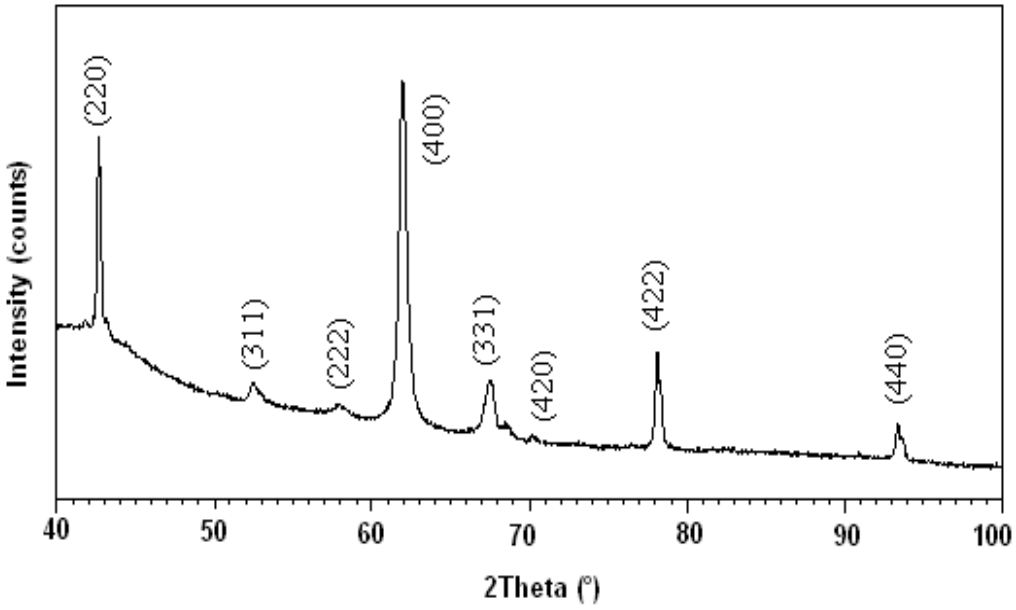

Figure 3. X-ray diffraction patterns for as-spun and annealed ribbons measured at RT.

3.3. Thermal Analysis

Figure 4 presents the thermal analysis curve of the as-spun and annealed ribbons using the DSC method. In the cooling and heating curves, it is observed that there are distinct exothermic and endothermic peaks that correlate to the martensitic transition. The temperatures for martensite start and finish and austenite start and finish are determined to be M_s = 300 K, M_f = 275 K, A_s = 293 K, and A_f = 310 K and M_s = K, M_f = K, A_s = K, and A_f = K. Sharmaa and Suresh [27] recently reported the characteristic martensitic transformation temperatures for ternary $Mn_{50}Ni_{40}Sn_{10}$ ribbons, which they determined to be M_s = 223 K, M_f = 182 K, A_s = 190 K, and A_f = 227 K. On the other hand, the transition temperatures for ternary $Mn_{50}Ni_{41}Sn_9$ ribbons were similarly established by Zhida Han et al. [28] as M_s = 300 K, M_f = 280 K, A_s = 290 K, and A_f = 320 K.

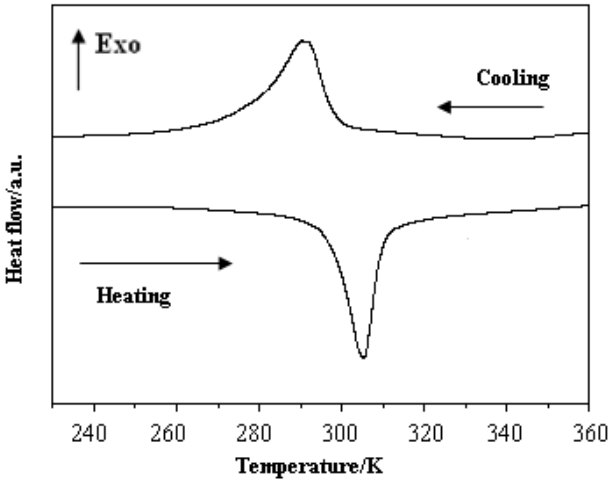

Figure 4. DSC cyclic scan for the as-spun and annealed ribbons obtained at a heating/cooling rate of 10 K min^{-1}. Arrows indicate cooling and heating.

The rise in elastic and surface energy during the development of martensite may be the cause of the measured hysteresis. Thus, supercooling is implied by the martensite's nucleation. The difference in temperatures at the peak sites, ΔT ($\Delta T = A_s - M_f$), is used to calculate the width of the hysteresis. For this ribbon, a value of about 14 K was obtained after cooling and heating. The intersection of a baseline and the tangents to each peak were used to identify the beginning and ending temperatures of the change. This made it very evident that the structural transition from the austenite to the martensite phase upon cooling and the opposite transition upon heating were both first-order processes. The martensite transformation temperature T_0 (the temperature at which the Gibbs energies of the martensitic and parent phases are related to the M_s and A_f parameters by the equation $T_0 = 1/2(M_s + A_f)$ [29]) can also be used to describe the transformation area. In Table 1, the calculated value of T_0 is displayed. As seen, the value of T_0 decreases as cooling rates rise. In general, the evolution of the electron to the atomic ratio (e/a), the Mn–Mn interatomic distance, and grain size can be linked to variations in transition temperatures. The electron concentration has a significant influence on the characteristic temperatures, including martensitic structural and transition temperatures. The number of 3d and 4s electrons in Mn, Ni, and Sn, as well as the sum of the 5s and 5p electrons in Mn, gives rise to the valence electron numbers of 7, 10, and 4, respectively. Additionally, it should be emphasized that an MT for Ni–Mn–Sn systems can only occur in the electron concentration range of 8.0–8.2 [30]. However, it should be highlighted that an MT can only happen for Mn–Ni–Sn in the electron concentration range of 7.9–8.2 [24]. The average valence electrons per atom (e/a) parameter was added to further define this alloy. For the alloy $Mn_{51}Ni_{39}Sn_{10}$, the calculated value of (e/a) is equal to 7.87. Other Ni–Mn–(In,Sn) Heusler alloys showed comparable results [8,11]. Indeed, Heusler alloys' structural transition temperatures can be changed by doping or modifying the composition [31]. According to Sanchez-Alorcos et al. [32], the valence electron concentration (e/a ratio) affects the martensitic transition temperature.

Table 1. Structural transition temperatures and the calculated values of T_0 recorded at different cooling rates.

Rates (K/min)	M_s (±1) (K)	M_f (±1) (K)	A_s (±1) (K)	A_f (±1) (K)	T_0 (±1) (K)
10	300	275	293	310	305
15	298.13	273.98	290.3	310	304
20	296.89	269.24	290.3	311	303.9
30	295.9	267.1	293.84	311	303.45
40	295.54	266.2	296.4	311	303.27

3.4. Kinetics

The dependence of the MT temperature interval was determined using calorimetric experiments with cooling rates ranging from 10 to 40 K min^{-1} (Figure 5). Prior to the measurements, careful calibrations with various rates were carried out. It is obvious that when cooling rates rise, the MT peak changes to lower temperatures. This effect is slightly more pronounced for greater cooling rates. It is clear that M_s and M_f both diminish as the cooling rate rises, but M_s exhibits a considerably larger reliance that may also result from the DSC sample's slow thermal conduction. Similar results were reported most recently by Zheng et al. and Bachaga et al. [33,34].

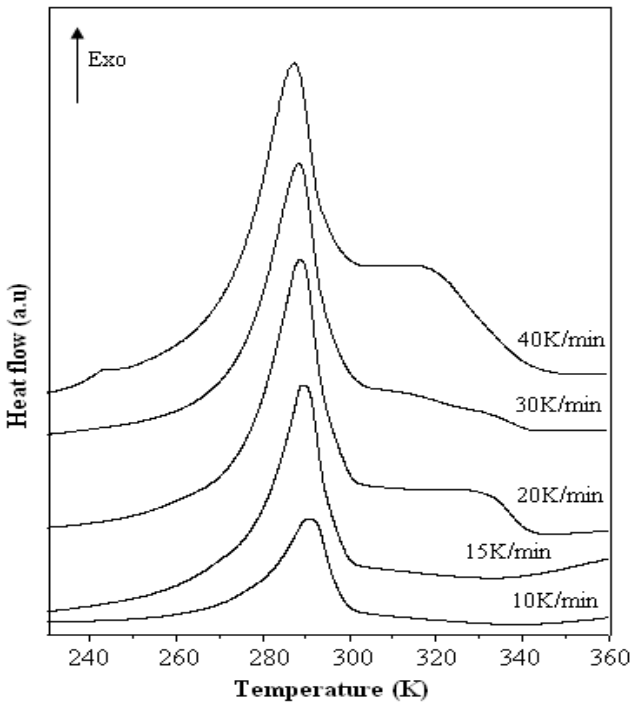

Figure 5. DSC charts of (Mn,Ni)Sn annealed ribbons recorded at different cooling rates of 10, 15, 20, 25, 30, and 40 K min^{-1}.

Based on the current result that the austenite phase's crystal structure is cubic $L2_1$, it is crucial to investigate the transformation's kinetics, specifically the activation energy, in order to gain a thorough understanding of the theoretical basis of MT. By investigating this, heat-treatment parameters may be adjusted. It is evident that when the cooling rate increases, the corresponding MT temperature decreases and the transition temperature range tends to widen. The Kissinger relation [35–37] can be used to obtain a transition parameter, as shown below:

$$\ln\left(\frac{B}{T^2}\right) = \frac{-Ea}{RT} + cte$$

where R is the gas constant, B is the cooling rate, T is the transition peak temperature, and c is the constant coefficient. In heating experiments, Ea is considered the average activation energy of the process. Nevertheless, in cooling experiments, this interpretation is doubtful. Tranchida et al. [38] consider Ea/R as a phenomenological parameter to obtain information about transformation tendencies. In this work, we applied Ea as a phenomenological parameter to check the cooling trend as well as to compare its values with the scientific literature. The slope of the plots of Ln (B/T^2) vs. $1/T$ shown in Figure 6 is used to calculate the value of Ea for annealed ribbons processed at various cooling rates using the approach described above. The relationship between Ln (B/T^2) and $1/T$ can be plotted linearly, and the calculated value of Ea is approximately 331.46 (0.02) kJ mol^{-1}. This value is comparable to that determined for the $Ni_{49}Mn_{39}Sn_{12}$ ribbons by Zheng et al. [33].

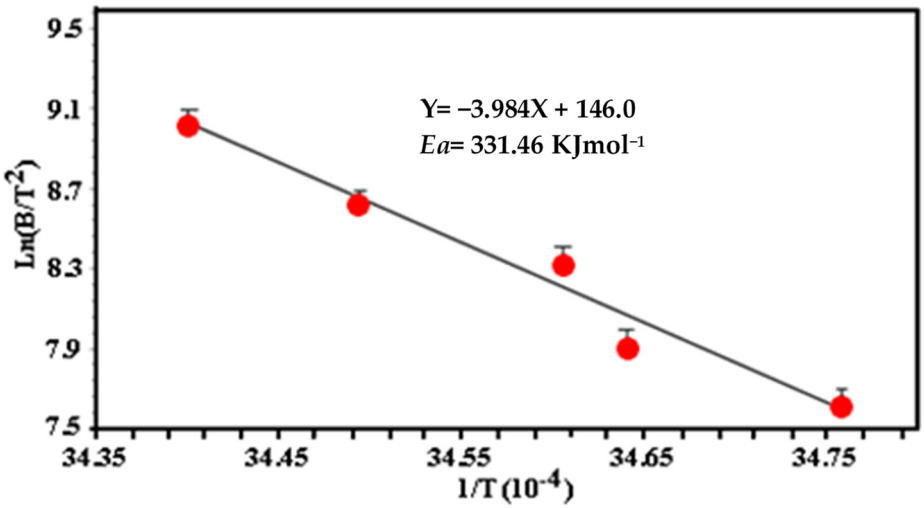

Figure 6. The Ln (B/T^2) vs. $1/T$ plot at different cooling rates of annealed ribbons.

Numerous studies have used Kissinger or Kissinger-like methods [39] to determine the MT and precipitation kinetics of various compositions with first-order transformation, such as Ti–Al–V [40], Cu–Ni–Al [41,42], and Fe–C(N) [43–45], as well as the ordering transition kinetics in Ni–Mn–Ga [36]. These studies were based on calorimetric results. The slope of linear curves of Ln (B/T^2) vs. $1/T$ appears to have a critical point, as reported by Fernandez et al. [46], who attributed this phenomenon to estimated error. For 50.8 at.% Ni–Ti SMA, Hsu et al. [46] discovered that martensitic substructure could change from coarse twins to fine twins or stacking faults with variations in cooling speeds varying from 0.5 to 25 K min^{-1}. Additionally, stacking faults in the plane (001) surface with a low cooling rate have an atomic displacement that is twice as large as stacking faults with a higher cooling rate. Due to the fact that twinning and atomic displacements in the MT process significantly increase at relatively low cooling rates, an increase in activation energy is required for the transition results, which is likely the cause of the rate dependency of activation energy in our work. The only factor affecting the phase interface velocity is supercooling, which causes the temperature rate to drop to extremely low levels [47]. Because slow cooling is responsible for a stronger chemical driving force and, thus, a lower activation energy, rapid cooling of the alloy would enable more supercooling in a shorter amount of time. The varied crystal structures related to varying cooling rates around the critical rate may also be a contributing factor, which leads to different activation energies being induced. It is likely that cooling the sample at a rate lower than the critical rate will make it easier for local or even long-term atomic diffusion, which could result in the appearance of a different variety of martensitic structure from that produced by cooling at a high rate or a non-martensite structure. However, it is not yet clear what exactly causes the rate of dependence. Researchers are still working to update some of these secrets, which demands more investigation.

4. Conclusions

In summary, the effect of annealing on the microstructure, structural, and MT of $Mn_{51}Ni_{39}Sn_{10}$ (at.%) shape memory alloy was studied. On the basis of the experimental results obtained, some conclusions can be cited.

- A cubic $L2_1$ structure was detected, at RT, for both alloys.
- The phase transformation temperatures increased remarkably after annealing.
- A high dependence between the cooling rates and the *Ea* was detected.

Author Contributions: Conceptualization, M.K. and J.-J.S.; formal analysis, H.R. and M.C.; data curation, B.H.; writing—original draft preparation, H.R., T.B. and B.H.; writing—review and editing; supervision, M.K. and J.-J.S. All authors have read and agreed to the published version of the manuscript.

Funding: This research received no external funding.

Institutional Review Board Statement: Not applicable.

Informed Consent Statement: Not applicable.

Data Availability Statement: Data can be requested from the authors.

Conflicts of Interest: The authors declare no conflict of interest.

References

1. Krenke, T.; Acet, M.; Wassermann, E.F.; Moya, X.; Mañosa, L.; Planes, A. Martensitic transitions and the nature of ferromagnetism in the austenitic and martensitic states of Ni-Mn-Sn alloys. *J. Phys. Rev. B* **2005**, *72*, 014412. [CrossRef]
2. Zhao, X.G.; Hsieh, C.C.; Lai, J.H.; Cheng, X.J.; Chang, W.C.; Cui, W.B. Effects of annealing on the magnetic entropy change and exchange bias behavior in melt-spun Ni-Mn-In ribbons. *J. Scr. Mater.* **2010**, *63*, 250–253. [CrossRef]
3. Zheng, H.X.; Wu, D.Z.; Xue, S.C.; Frenzel, J.; Eggeler, G.; Zhai, Q.J. Martensitic transformation in rapidly solidified Heusler Ni49Mn39Sn12 ribbons. *J. Acta Mater.* **2011**, *59*, 5692–5699. [CrossRef]
4. Raj Kumar, D.M.; Sridhara Rao, D.V.; Rama Rao, N.V.; Manivel Raja, M.; Singh, R.K.; Suresh, K.G. In-situ phase transformation studies of Ni48Mn39In13 melt-spun ribbons. *J. Intermet.* **2012**, *25*, 126–130. [CrossRef]
5. Krenke, T.; Moya, X.; Aksoy, S.; Acet, M.; Entel, P.; Manosa, L.; Planes, A.; Elerman, Y.; Yücel, A.; Wassermann, E.F. Electronic aspects of the martenistic transition in Ni-Mn based Heusler alloys. *J. Magn. Magn. Mater.* **2007**, *310*, 2788–2789. [CrossRef]
6. Sánchez Llamazares, J.L.; Sanchez, T.; Santos, J.D.; Pérez, M.J.; Sanchez, M.L.; Hernando, B. Martensitic phase transformation in rapidly solidified Mn50Ni40In10 alloy ribbons. *J. Appl. Phys. Lett.* **2008**, *92*, 012513. [CrossRef]
7. Xuan, H.; Xie, K.; Wang, D.; Han, Z.; Zhang, C.; Gu, B. Effect of annealing on the martensitic transformation and magnetocaloric effect in Ni44.1Mn44.2Sn11.7 ribbons. *J. Appl. Phys. Lett.* **2008**, *92*, 242506. [CrossRef]
8. Hernando, B.; Sánchez Llamazares, J.L.; Santos, J.D.; Escoda, L.; Suñol, J.J.; Varga, R.; Baldomir, D.; Serantes, D. Thermal and magnetic field-induced martensite-austenite transition in Ni50.3Mn35.3Sn14.4 ribbons. *J. Appl. Phys. Lett.* **2008**, *92*, 042504. [CrossRef]
9. Anantharman, T.R.; Suryanarayana, C. *Rapidly Solidified Metals: A Technological Overview*; Trans Tech Publications: Pfaffikon, Switzerland, 1987.
10. Hernando, B.; Sanchez Llamazares, J.L.; Prida, V.M.; Baldomir, D.; Serantes, D.; Ilyn, M. Magnetocaloric effect in preferentially textured Mn50Ni40In10 melt spun ribbons. *J. Appl. Phys. Lett.* **2009**, *94*, 222502. [CrossRef]
11. Krenke, T.; Duman, E.; Acet, M.; Wassermann, E.F.; Moya, X.; Mañosa, L. Inverse magnetocaloric effect in ferromagnetic Ni-Mn-Sn alloys. *J. Nat. Mater.* **2005**, *4*, 450–454. [CrossRef]
12. Santos, J.D.; Sanchez, T.; Alvarez, P.; Sanchez, M.L.; Sanchez Llamazares, J.L.; Hernando, B. Microstructure and magnetic properties of Ni50Mn37Sn13 Heusler alloy ribbons. *J. Appl. Phys.* **2008**, *103*, 07B326. [CrossRef]
13. Feng, Y.; Sui, J.H.; Chen, L.; Cai, W. Martensitic transformation behaviors and magnetic properties of Ni-Mn-Ga rapidly quenched ribbons. *J. Mater. Lett.* **2009**, *63*, 965–968. [CrossRef]
14. Manosa, L.; Moya, X.; Planes, A.; Gutfleisch, O.; Lyubina, J.; Barrio, M.; Tamarit, L.; Aksoy, S.; Krenke, T.; Acet, M. Effects of hydrostatic pressure on the magnetism and martensitic transition of Ni-Mn-In magnetic superelastic alloys. *J. Appl. Phys. Lett.* **2008**, *92*, 012515. [CrossRef]
15. Wang, D.; Zhang, C.; Han, Z.; Xuan, H.; Gu, B.; Du, Y. Large magnetic entropy changes and magnetoresistance in Ni45Mn42Cr2Sn11 alloy. *J. Appl. Phys.* **2008**, *103*, 033901. [CrossRef]
16. Krenke, T.; Duman, E.; Acet, M.; Moya, X.; Manosa, L.; Planes, A. Effect of Co and Fe on the inverse magnetocaloric properties of Ni-Mn-Sn. *J. Appl. Phys.* **2007**, *102*, 033903. [CrossRef]
17. Liu, J.; Scheerbaum, N.; Hinz, D.; Gutfleisch, O. Magnetostructural transformation in Ni-Mn-In-Co ribbons. *J. Appl. Phys. Lett.* **2008**, *92*, 162509. [CrossRef]
18. Wang, D.H.; Zhang, C.L.; Xuan, H.C.; Han, Z.D.; Zhang, J.R.; Tang, S.L.; Gu, B.X.; Du, Y.W. The study of low-field positive and negative magnetic entropy changes in Ni43Mn46−xCuxSn11 alloys. *J. Appl. Phys.* **2007**, *102*, 013909. [CrossRef]
19. Moya, X.; Manosa, L.; Planes, A.; Krenke, T.; Acet, M.; Wassermann, E.F. Lattice dynamics of Ni–Mn–Al Heusler alloys. *J. Mater. Sci. Eng. A* **2006**, *481–482*, 227–230. [CrossRef]
20. Yuhasz, W.M.; Schlagel, D.L.; Xing, Q.; McCallum, R.W.; Lograsso, T.A. Metastability of ferromagnetic Ni–Mn–Sn Heusler alloys. *J. Alloys Compd.* **2010**, *492*, 681–684. [CrossRef]
21. Xuan, H.C.; Deng, Y.; Wang, D.H.; Zhang, C.L.; Han, Z.D.; Du, Y.W. Effect of annealing on the martensitic transformation and magnetoresistance in Ni–Mn–Sn ribbons. *J. Phys. D Appl. Phys.* **2008**, *41*, 215002. [CrossRef]

22. Hernando, B.; Sanchez-Llamazares, J.L.; Santos, J.D.; Prida, V.M.; Baldomir, D.; Serantes, D.; Varga, R.; González, J. Magnetocaloric effect in melt spun Ni50.3Mn35.5Sn14.4 ribbons. *Appl. Phys. Lett.* **2008**, *92*, 132507. [CrossRef]
23. Lutterotti, L.; MAUD; CPD. (IUCr), No. 24. 2000. Available online: http://www.iucr.org/iucr-top/comm/cpd/Newsletters/Newsletter (accessed on 19 October 2022).
24. Coll, R.; Escoda, L.; Saurina, J.; Sanchez-Llamazares, J.L.; Hernando, B.; Sunol, J.J. Martensitic transformation in Mn–Ni–Sn Heusler alloys. *J. Therm. Anal. Calorim.* **2010**, *99*, 905–909. [CrossRef]
25. Rekik, H.; Chemingui, M.; Marzouki, A.; Bosh, E.; Escoda, L.; Sunol, J.J.; Khitouni, M. Structural and Magnetic Changes due to the Martensitic Transformation in Rapidly Solidified Ni50Mn37Sn6.5In6.5 Ribbons. *J. Supercond. Nov. Magn.* **2015**, *28*, 2165–2170. [CrossRef]
26. Bachaga, T.; Rekik, H.; Krifa, M.; Sunol, J.J.; Khitouni, M. Investigation of the enthalpy/entropy variation and structure of Ni–Mn–Sn (Co, In) melt-spun alloys. *J. Therm. Anal. Calorim.* **2016**, *126*, 1463–1468. [CrossRef]
27. Sharmaa, J.; Suresh, K.G. Investigation of multifunctional properties of Mn50Ni40−xCoxSn10 (x = 0–6) Heusler alloys. *J. Alloys Compd.* **2015**, *620*, 329–336. [CrossRef]
28. Han, Z.; Chen, X.; Zhang, Y.; Chen, J.; Qian, B.; Jiang, X.; Wang, D.; Du, Y. Martensitic transformation and magnetocaloric effect in Mn–Ni–Nb–Sn shape memory alloys: The effect of 4d transition-metal doping. *J. Alloys Compd.* **2012**, *515*, 114. [CrossRef]
29. Kaufman, L.; Hullert, M. Thermodynamics of martensite transformation. In *Martensite*; Olson, G.B., Owen, W.S., Eds.; ASM International: Cambridge, UK, 1992; pp. 41–58.
30. Schlagel, D.L.; Yuhasz, W.M.; Dennis, K.W.; McCallum, R.W.; Lograsso, T.A. Temperature dependence of the field-induced phase transformation in Ni50Mn37Sn13. *J. Scr. Mater.* **2008**, *59*, 1083. [CrossRef]
31. Planes, A.; Manosa, L.; Acet, M. Magnetocaloric effect and its relation to shape-memory properties in ferromagnetic Heusler alloys. *J. Phys. Condens. Matter.* **2009**, *21*, 233201. [CrossRef]
32. Sanchez-Alarcos, V.; Recarte, V.; Perez-Landazabal, J.I.; Gomez-Polo, C.; Rodriguez-Velamazan, J.A. Role of magnetism on the martensitic transformation in Ni–Mn-based magnetic shape memory alloys. *J. Acta. Mater.* **2012**, *60*, 459–468. [CrossRef]
33. Zheng, H.; Wang, W.; Wu, D.; Xue, S.; Zhai, Q.; Frenzel, J.; Luo, Z. Athermal nature of the martensitic transformation in Heusler alloy Ni–Mn–Sn. *J. Intermet.* **2013**, *36*, 90–95. [CrossRef]
34. Bachaga, T.; Zhang, J.; Ali, S.; Sunol, J.J.; Khitouni, M. Impact of annealing on martensitic transformation of Mn50Ni42.5Sn7.5 shape memory alloy. *Appl. Phys. A* **2019**, *125*, 146. [CrossRef]
35. Kissinger, H.E. Variation of Peak Temperature with Heating Rate in Differential Thermal Analysis. *J. Res. Natl. Bur. Stand.* **1956**, *57*, 217–221. [CrossRef]
36. Kostov, A.I.; Zivkovic, Z.D. Thermodilatometry investigation of the martensitic transformation in copper-based shape memory alloys. *J. Thermochim. Acta* **1997**, *291*, 51–57. [CrossRef]
37. Fernandez, J.; Benedetti, A.V.; Guilemany, J.M.; Zhang, X.M. Thermal stability of the martensitic transformation of Cu–Al–Ni–Mn–Ti. *J. Mater. Sci. Eng. A* **2006**, *723*, 438–440. [CrossRef]
38. Tranchida, D.; Gloger, D.; Gahleitner, M. A critical approach to the Kissinger analysis for studying non-isothermal crystallization of polymers. *J. Therm. Anal. Calorim.* **2017**, *129*, 1057–1064. [CrossRef]
39. Malinov, S.; Guo, Z.; Sha, W.; Wilson, A. Differential scanning calorimetry study and computer modeling of β ⇒ α phase transformation in a Ti-6Al-4V alloy. *J. Met. Mater. Trans. A* **2001**, *32*, 879. [CrossRef]
40. Lipe, T.; Morris, M.A. Effect of thermally activated mechanisms on the martensitic transformation of modified Cu-Al-Ni alloys. *J. Acta. Met. Mater.* **1995**, *43*, 1293–1303. [CrossRef]
41. Recarte, V.; Pérez-Landazabal, J.I.; Ibarra, A.; No, M.L.; Juan, J.S. High temperature β phase decomposition process in a Cu–Al–Ni shape memory alloy. *J. Mater. Sci. Eng. A* **2004**, *378*, 238–242. [CrossRef]
42. Liu, C.; Brakman, C.M.; Korevaar, B.M.; Mittemeijer, E.J. The tempering of iron- carbon martensite; dilatometric and calorimetric analysis. *J. Met. Trans. A* **1988**, *19*, 2415–2426.
43. Guo, Z.; Sha, W.; Li, D. Quantification of phase transformation kinetics of 18 wt.% Ni C250 maraging steel. *J. Mater Sci. Eng. A* **2004**, *373*, 10–20. [CrossRef]
44. Mittemeijer, E.J.; Van Gent, A.; Van Der Schaaf, P. Analysis of transformation kinetics by nonisothermal dilatometry. *J. Met. Mater. Trans. A* **1986**, *17*, 1441–1445. [CrossRef]
45. Vazquez, J.; Villares, P.; Jiménez-Garay, R. A theoretical method for deducing the evolution with time of the fraction crystallized and obtaining the kinetic parameters by DSC, using non-isothermal techniques. *J. Alloys Compd.* **1997**, *257*, 259–265. [CrossRef]
46. Hsu, T.Y. *Martensitic Transformation and Martensite*; Science Press: Beijing, China, 1999; Chapter 1.
47. Ostuka, K.; Ren, X.; Takeda, T. Experimental test for a possible isothermal martensitic transformation in a Ti-Ni alloy. *J. Scr. Mater.* **2001**, *45*, 145–152.